



**HAL**  
open science

# Insights into the Rheological Behavior of Aqueous Dispersions of Synthetic Saponite: Effects of Saponite Composition and Sodium Polyacrylate

Cunjun Li, Qiqi Wu, Sabine Petit, Will Gates, Huimin Yang, Weihua Yu, Chunhui Zhou

► **To cite this version:**

Cunjun Li, Qiqi Wu, Sabine Petit, Will Gates, Huimin Yang, et al.. Insights into the Rheological Behavior of Aqueous Dispersions of Synthetic Saponite: Effects of Saponite Composition and Sodium Polyacrylate. *Langmuir*, 2019, 35 (40), pp.13040-13052. 10.1021/acs.langmuir.9b01805 . hal-02363075

**HAL Id: hal-02363075**

<https://cnrs.hal.science/hal-02363075v1>

Submitted on 3 Dec 2020

**HAL** is a multi-disciplinary open access archive for the deposit and dissemination of scientific research documents, whether they are published or not. The documents may come from teaching and research institutions in France or abroad, or from public or private research centers.

L'archive ouverte pluridisciplinaire **HAL**, est destinée au dépôt et à la diffusion de documents scientifiques de niveau recherche, publiés ou non, émanant des établissements d'enseignement et de recherche français ou étrangers, des laboratoires publics ou privés.



39 and altered the thixotropic properties such that the hydrogel becomes a sol. The addition of NaPA  
40 facilitated the dispersion and delamination of Sap, because under the electric field of negatively  
41 charged Sap particles in the hydrogel, the anionic NaPA was instantaneously polarized and thereby  
42 entered the hydration layer of the Sap particles.

## 50 1. Introduction

51 Saponite (Sap) is a 2:1 trioctahedral clay mineral. A layer of Sap is composed of two sheets  
52 of hexagonally arrayed [SiO<sub>4</sub>] tetrahedra sandwiching a central sheet of [MgO<sub>4</sub>(OH)<sub>2</sub>] octahedra.  
53 A small amount of isomorphous substitution of Si<sup>4+</sup> for Al<sup>3+</sup> (and sometimes other trivalent  
54 cations such as Fe<sup>3+</sup>) in the tetrahedral sheet causes a negatively charged sheet. In many types of  
55 Sap, Al<sup>3+</sup> or Fe<sup>3+</sup> can substitute Mg<sup>2+</sup> in the octahedral sheet, creating a positive octahedral  
56 sheet charge; however, substitution in the tetrahedral results in an overall negative net charge of  
57 the 2:1 layer.<sup>1</sup> The negative layer charge is compensated by exchangeable cations such as Na<sup>+</sup> ,  
58 NH<sub>4</sub><sup>+</sup> , K<sup>+</sup> , Li<sup>+</sup> , and Mg<sup>2+</sup>, which reside in the (generally) hydrated interlayer. An ideal  
59 structural formula of Sap is thus described as M<sub>x/z</sub> z<sup>+</sup> [Mg<sub>6</sub>][Si<sub>8-x</sub>Al<sub>x</sub>]O<sub>20</sub>(OH)<sub>4</sub>·nH<sub>2</sub>O, where  
60 M<sub>z</sub><sup>+</sup> represents the interlayer cations, x ranges from approximately 0.4– 1.2, and n represents the  
61 number of surface- and/or cation hydration water molecules.<sup>2</sup> Compared to montmorillonite, Sap  
62 generally has a smaller particle size and higher thermal stability.<sup>3</sup> In particular, Sap can be more  
63 readily delaminated and exfoliated into nanoplatelets or even single nanolayers in water.<sup>4</sup> As is  
64 typical of high swelling smectites, in aqueous dispersion, its solid–water interfacial properties  
65 enable it to form colloidal sols or gels. For this reason, Sap has been used for many decades as a  
66 nontoxic thickener,<sup>5</sup> plasticizer,<sup>6</sup> or emulsifier<sup>7</sup> in products such as paint, plaster, cosmetics,  
67 personal care products, and adhesives.<sup>8</sup> Naturally occurring saponite deposits are scarce and  
68 generally contain mineral and metal impurities, and hence laborious and time-consuming  
69 purification is required.<sup>9</sup> This limitation restricts the use of natural Sap; the potential of its  
70 synthetic counterparts in industrial applications is therefore of interest. The technology of  
71 synthesizing Sap-like clay minerals with a well-controlled chemical composition has been  
72 successfully developed, and the products are generally referred to as a synthetic Sap (Sap). In the  
73 past, three successful approaches in the synthesis of Sap have been applied:  
74 microwave-assisted,<sup>10</sup> nonhydrothermal,<sup>11,12</sup> and hydrothermal.<sup>13,14</sup> The microwave-assisted  
75 method is conducive to reduction of synthesis time and control of the structure with large pores  
76 and high specific surface area.<sup>15,16</sup> To make the process rapid and feasible in industrial-scale, the

77 nonhydrothermal method under mild condition was developed.<sup>12,17</sup> Typically, a gel containing  
78 the source of Si, Al, and Na was first prepared at room temperature, followed by mixing it with a  
79 solution of urea and metal salts (introducing special metal cations, such as Co and Ni). In this way,  
80 the octahedral sheets of saponites can be easily designed to contain one or more of different metal  
81 cations. As the hydrothermal method requires only relatively simple equipment and the reaction  
82 conditions are easy to control with precision, it is the frequently used approach for Sap  
83 synthesis.<sup>13</sup> For many industrial applications, Sap (whether synthetic or natural) commonly needs  
84 surface engineering (functionalization), such as intercalation and/or hybridization to enhance its  
85 reactivity. Recently, various new Sap-based functional materials, such as nanoparticles/Sap  
86 hydrogels, surface-functionalized Sap, and inorganically modified and hybridized Sap, were  
87 designed to produce new functional materials. These Sap-based functional materials may exhibit  
88 exceptional biological, electrical, and optical properties and applied in electromagnetic,  
89 magnetorheological, catalytic, and biological fields.<sup>18–20</sup> Such functionalization is usually  
90 conducted in aqueous dispersions. In addition, electrolytes are frequently added to adjust the  
91 rheological performance of the Sap-based products in practice. Therefore, understanding the  
92 physical and chemical interactions between Sap and electrolytes in an aqueous dispersion is  
93 critical and fundamental. Deep experimental and theoretical understanding of the rheological  
94 behavior of aqueous dispersions of synthetic saponite is worthwhile. Aqueous dispersions and  
95 hydrogels of Sap can exhibit different physical states, for example, stable colloidal dispersion or  
96 viscoelastic sol and elastic solids.<sup>21,22</sup> The rheological properties of Sap hydrogels are related to  
97 electrolyte concentration.<sup>23</sup> Shear thinning is a common phenomenon for flocs/aggregates that  
98 break down when shear is applied. However, shear thickening is uncommon for most clay  
99 dispersions and implies that energy input is dissipated into enhanced gels. Thixotropy is the  
100 hysteresis in shear stress between increasing and decreasing shear rate paths. Most clay gels  
101 undergo shear thinning with increasing shear rate but some thickening when the shear rate  
102 decreases after a prolonged exposure to a high shear rate. The Sap hydrogel system, at  
103 concentrations less than 1.1 wt % of solid content, displays a typical Newtonian flow, but at  
104 concentrations exceeding 1.2 wt %, it can exhibit distinct shear thinning.<sup>24</sup> Aspects of how the  
105 chemical composition and crystallinity of Sap affect the complex rheological behavior of Sap  
106 hydrogels remain elusive. For the purpose of tuning the shear thinning of Sap dispersions for  
107 different applications, electrolytes or polyelectrolytes can generally be introduced to help  
108 dispersion,<sup>25</sup> stabilization,<sup>26</sup> or flocculation of clay mineral suspensions.<sup>27</sup> Sodium polyacrylate  
109 (NaPA, denoted SN-5040 in the industry) is one of the most frequently used polyelectrolytes in  
110 paints, pigments, and waste water treatment.<sup>28,29</sup> Therefore, the thixotropy of Sap dispersion is a  
111 major factor affecting the workability of these products. However, details regarding thixotropic  
112 interactions with Sap in water have been rarely reported and rheological behaviors of aqueous  
113 Sap-NaPA dispersions are unknown. The objective of this work is to correlate the rheological

114 behavior of Sap hydrogels as a function of the chemical composition of Sap and load rates of  
115 NaPA.

116

## 117 **2.Experimental Section**

### 118 **2.1 Synthesis of saponite**

119 The synthesis procedure was as follows: a mixture of 36.3 g of NaOH and 65.6 g of NaHCO<sub>3</sub> was  
120 dissolved in 500 mL of deionized water to develop solution A. Then, 88.83 g of sodium silicate  
121 was added in 490 mL of solution A under vigorous stirring to create solution B. A given amount of  
122 MgCl<sub>2</sub>·6H<sub>2</sub>O and AlCl<sub>3</sub>·6H<sub>2</sub>O was dissolved in 175 mL of deionized water (solution C) to  
123 provide a range of Si/Al in the final product. Under continuous stirring, solution C was slowly  
124 added into solution B until a uniform white suspension was observed. The suspension was then  
125 transferred to a polytetrafluoroethylene-lined autoclave and heated at 200 °C for 24 h. The solid  
126 phase was washed with deionized water to eliminate chlorides and finally dried at 90 °C in an  
127 oven and ground in a mortar. The obtained product was denoted Sap<sub>x</sub>, where x represents the  
128 Si/Al molar ratio. For example, Sap<sub>5</sub> means the Sap synthesized at the Si/Al molar ratio of 5.

### 129 **2.2. Preparation of Sap Hydrogels and NaPA-Loaded Sap Dispersion**

130 Sap<sub>x</sub> (2.47 g) was added into 80 mL of deionized water, and the mixture was stirred to form a  
131 suspension (3 wt % Sap). A total of 30 mL of suspension was then transferred to a tube, and the  
132 remaining 50 mL of suspension was transferred and divided into five tubes with an equal volume  
133 of 10 mL. After standing for 7 d at room temperature, Sap hydrogels were obtained. For the  
134 preparation of NaPA-loaded Sap dispersion, 0.25, 0.50, 0.75, 1.0, and 1.25 mL NaPA solution (4  
135 g/L) was added into the above five 10 mL tubes separately. The corresponding mixtures of  
136 different concentrations were denoted Sap<sub>x</sub>-NaPA<sub>y</sub>, where x represents the Si/Al ratio of the  
137 dispersed Sap at 5, 10, 15, 20, or 25 and y is the concentration of added NaPA at 0.10, 0.19, 0.28,  
138 0.36, or 0.44 g/L aqueous Sap dispersion. For example, Sap<sub>20</sub>-NaPA<sub>0.44</sub> indicates that the  
139 mixture was made by Sap<sub>20</sub> with a concentration of NaPA at 0.44 g/L. To study the structure of  
140 the Sap after dispersion in the presence of NaPA, Sap<sub>x</sub>-NaPA<sub>0.44</sub> (the concentration of NaPA in  
141 Sap<sub>x</sub> dispersion is 0.44 g/L) was dried at 80 °C to a constant weight. For comparison, Sap  
142 dispersions without adding NaPA were dried under the same conditions and used as a control.  
143 Such a sample was denoted Sap<sub>x</sub>control.

144

### 145 **2.3 Powder X-ray Diffraction (XRD) and X-ray Fluorescence (XRF)**

146 Powder X-ray diffraction (XRD) analysis was carried out on an X-ray diffractometer (X'Pert PRO,  
147 PANalytical, The Netherlands). Cu target K $\alpha$  ( $\lambda = 0.154056$  nm), a voltage of 40 kV, a current of

148 40 mA, and a scanning range of 2–80° were used. Elemental analyses of the samples (pressed  
149 powders) were carried out using an ARL ADVANT’X IntelliPower™ 4200 sequential X-ray  
150 fluorescence (XRF) analyzer. The layer charge density calculation of the structural formula was  
151 based on well-known assumptions about the structure of Sap (2:1 layer structure, 22 oxygen  
152 equivalence, all Mg assigned to an octahedral sheet, etc.).<sup>30</sup>

### 153 **2.3 Fourier infrared spectroscopy (FTIR)**

154 Fourier transform infrared spectra (FTIR) were recorded in transmission mode with a Nicolet  
155 6700 FTIR spectrometer (Thermoelectric Nicolet, United States). Pressed disk samples were  
156 prepared by mixing the powdered solids with KBr in a pelleting device. All samples were  
157 measured at a wavenumber range of 400–4000 cm<sup>-1</sup> with 32 scans. The wavenumber accuracy  
158 was better than 0.01 cm<sup>-1</sup>, and the resolution was better than 0.09 cm<sup>-1</sup>.

### 159 **2.4 Pore Structure Characterization**

160 The pore size distribution of Sap was detected on a Micromeritics ASAP2020 analyzer. Before the  
161 measurements, the Sap samples were degassed at 473 K for 10 h under a N<sub>2</sub> flow.

### 162 **2.5 Scanning Electron Microscopy (SEM)**

163

164 For SEM characterization, the powder sample was mounted onto a conductive adhesive, coated in  
165 gold, and then analyzed on a Hitachi S-4700(II) scanning electron microscope.

### 166 **2.6 Rheological measurement**

167 The rheological properties of the Sap hydrogels were measured using a Malvern Kinexus  
168 Rheometer (Malvern Kinexus Lab+ Rheometer). The flow measurements were carried out at 25 ±  
169 0.1 °C using a rotational rheometer with a CP4/ 40 SR71SS cone-plate sensor; oscillatory  
170 measurements were carried out over a frequency range of 0.1–10 Hz at 25 ± 0.1 °C using a stress  
171 control rheometer equipped with a CP4/40 SR71SS cone-plate sensor system. The data was  
172 analyzed using the rSpace software for the Kinexus rheometer.

### 173 **2.7 Zeta potential and dynamic light scattering (DLS) measurement**

174 . A fresh Sap dispersion was prepared by adding 1.22 g of Sap into 80 mL of deionized water. The  
175 zeta potential and particle size distribution of the synthetic saponite dispersion were performed  
176 with a Malvern Nano ZS90 instrument.

### 177 3. Results and Discussion

#### 178 3.1 Mineralogy of Sap

179 All synthetic samples (Figure 1c) exhibited reflections at  $2\theta$  6.03, 19.52, 29.04, 34.41, and 60.37°,  
180 corresponding to the (001), (0211), (004), (1320), and (060) reflections of saponite, respectively.<sup>4</sup>  
181 In particular, the position of the (060) reflection ( $d_{060}$  value) differentiates the structure of  
182 Al-enriched dioctahedral and Mg-enriched trioctahedral smectite.<sup>31</sup> The  $d_{060}$  value of the series  
183 of synthetic samples was 0.153 nm, indicating that the synthesized smectites have a trioctahedral  
184 structure (Figure 1a,b). This is in good agreement with the data reported in the literature that the  
185  $d_{060}$  of the trioctahedral structure is higher than 0.152 nm.<sup>32,33</sup> As such, in this work, Sap with  
186 Si/Al molar ratios of 5, 10, 15, 20, and 25 was successfully created with the hydrothermal process.  
187 The (001) reflections of the samples Sap5, Sap10, Sap15, Sap20, and Sap25 are 6.68, 6.13, 6.03,  
188 5.88, and 5.78°, corresponding to basal spacings of 1.33, 1.44, 1.46, 1.50, and 1.53 nm,  
189 respectively. As the Si/Al molar ratio increases from 5 to 25, theoretically, the layer charge  
190 decreases from 1.33 to 0.35 e/pfu (Table 1). Thus, the layer charge density decreases. Usually, the  
191 basal spacing of smectite is controlled by the attractive and repulsive forces between two adjacent  
192 layers.<sup>34</sup> As the layer charge increases, the electrostatic attraction increases more than the  
193 repulsive force.<sup>8</sup> Hence, the basal spacing followed the order Sap5 < Sap10 < Sap15 < Sap20 <  
194 Sap25. As the Si/Al molar ratio increased from 5 to 25, the intensity of the (001) and (004)  
195 reflections decreased, whereas their full widths at half-maximum (FWHM) significantly decreased  
196 (Figure 1c). A similar trend was also observed for the (060) and (100) reflections. These  
197 observations indicated that the synthetic saponites with a lower Si/Al ratio had superior  
198 crystallinity than those with a higher Si/Al ratio. Thus, a Si/Al molar ratio in the hydrothermal  
199 synthesis feedstock has a strong influence on the crystallinity of the resultant Sap. Decreasing the  
200 molar ratio of Si/Al favored Sap with larger crystal size and superior stacking order. As the Si/Al  
201 molar ratio inherently contributes to isomorphous substitution in the tetrahedral sheet of the  
202 saponite layer, greater content of Al in the tetrahedral sheet leads to superior crystallinity of the  
203 synthetic saponite.<sup>35</sup> The successful formation of Sap was also confirmed by FTIR spectroscopy  
204 (Figure 1d). The characteristic absorption bands<sup>36</sup> of Sap were observed at 3685, 1004, 800, 665,  
205 and 460  $\text{cm}^{-1}$ . The absorption band at 3685  $\text{cm}^{-1}$ , which arose from the stretching vibrational  
206 modes of Mg–OH, is a typical characteristic of trioctahedral clay minerals.<sup>37</sup> The broad band  
207 centered at 3440  $\text{cm}^{-1}$  and the band at 1645  $\text{cm}^{-1}$  were both due to adsorbed water molecules.  
208 The decrease of the band at 800  $\text{cm}^{-1}$ , due to tetrahedral Al–O vibrations from Sap5 to Sap25,  
209 indicated a decrease of the tetrahedral Al content according to the chemical composition of the  
210 synthetic saponites (Table 1). The band at 1058  $\text{cm}^{-1}$  reflects the stretching vibration of the  
211 Si–O–Si. The slight shift of this band from Sap5 to Sap25 also indicated a decrease of tetrahedral  
212 substitutions.<sup>38</sup>

213

## 214 3.2 Rheology of Sap

215 When a Sap is dispersed in water, it forms a colloid. In particular, the colloids of Sap10,  
216 Sap15, Sap20, and Sap25 appeared to be strongly optically transparent. After standing for 7 d,  
217 samples Sap10–Sap25 formed hydrogels (Figure S1aI). When the tubes were put upside down, the  
218 gels remained in place unless vibration (shear force) was applied. In contrast, Sap5 failed to form  
219 a hydrogel. This can be ascribed to the better crystallinity and higher layer charge of Sap5. In  
220 addition, the average particle size of the Sap5 is 2–3 times larger than that of the other Sap (Table  
221 1). Such Sap easily sedimented in suspension. The better crystallinity and layer charge make it  
222 difficult to delaminate; thus, it failed to form stable dispersions. Due to Tyndall scattering, a bright  
223 path in the hydrogels (Figure 2cI) of Sap10, Sap15, Sap20, and Sap25 can be observed. This  
224 suggests that the Sap had delaminated in the aqueous dispersion because of the electrostatic  
225 repulsion of Sap particles and thus existed as nanoparticles. Only colloids of Sap5 kept the form of  
226 a sol and did not form a gel. Thus, the rheological properties of Sap5 were not measured in the  
227 following experiments. Under a nonsteady state, the viscosity of the Sap hydrogel (3 wt %) as a  
228 function of shear rate (Figure 2a) suggested that the hydrogels showed distinct shear-thinning  
229 behaviors. At the lowest shear rate of  $0.1 \text{ s}^{-1}$ , the viscosities of the Sap hydrogels of Sap10,  
230 Sap15, Sap20, and Sap25 were 132.3, 149.6, 241.8, and 306.2 Pa·s, respectively. As the shear rate  
231 increased to  $100 \text{ s}^{-1}$ , the viscosity decreased. At a fast decrease from  $0.1$  to  $2.512 \text{ s}^{-1}$ , the  
232 viscosity decreased rapidly, and finally, the viscosity reached a minimum and tended to be equal  
233 for all four samples. A possible reason for the observed decrease of viscosity with increasing shear  
234 rate was that the house-of-card structure, with edge-to-face interactions between Sap nanolayers,  
235 was destroyed by shear force,<sup>39</sup> causing the direction of the delaminated layer of Sap in the  
236 hydrogel to gradually change to the direction of flow under shear force, resulting in the decreasing  
237 viscosity. At a shear rate of  $100 \text{ s}^{-1}$ , the viscosity of the aqueous Sap dispersions approached zero,  
238 revealing a typical shear-thinning process. The solidlike gel thus transformed to liquidlike sol at  
239 the highest shear rates. At a given shear rate, Sap samples with a higher layer charge density had  
240 lower-viscosity hydrogels. Sap20 and Sap25 resulted in hydrogels with greater swelling. A similar  
241 conclusion that greater charge density led to stronger cohesive strength between the layers, thus  
242 decreasing swelling, was also drawn in the literature.<sup>40</sup> Thus, that the layer charges of 0.53 e/pfu  
243 (Sap15) to 0.35 e/pfu (Sap25) resulted in greater swelling is a well-accepted deduction. Generally,  
244 because the Sap particles delaminate to isolated mono, or at least partially, delaminated  
245 multilayers, the increase in layer charge resulted in less delamination of Sap particles.<sup>41</sup>  
246 Experimental results of shear rate versus viscosity can be fitted to the Sisko<sup>42</sup> model (Figure S1a).  
247  $\eta = \eta_{\infty} + k\dot{\gamma}^{n-1}$ , where  $\eta_{\infty}$  denotes the infinite-rate viscosity in Pa·s,  $k$  is a constant,  $n$  is a rate  
248 index, and  $\dot{\gamma}$  represents shear rate. At a low shear rate, the house-of-card structure of Sap in a  
249 hydrogel strongly hinders rotation, thus requiring appreciable torque to initiate flow with the  
250 rotational rheometer. However, the house-of-card structure was destroyed gradually as the shear



251 rate increased. According to the Sisko model, at a shear rate of  $100 \text{ s}^{-1}$ , the Sap hydrogel  
252 approached infinite viscosity ( $\eta\infty$ ).

253 Shear stress, as a function of the shear rate (Figure 2b) of Sap (Sap10, Sap15, Sap20, and Sap25)  
254 hydrogels (3 wt %), showed similar behavior to non-Newtonian fluids.<sup>43</sup> At a shear rate of  $0.1$   
255  $\text{s}^{-1}$ , the shear stresses of the hydrogels of Sap10 and Sap15 were 13.24 and 14.96 Pa, whereas the  
256 shear stresses of Sap20 and Sap25 were 24.18 and 32.94 Pa, respectively. The data indicated that  
257 shear stress is closely related to the layer charge density of Sap. The shear stress increased with  
258 the decrease of layer charge density from Sap10 to Sap25. Inherently, higher shear stress means  
259 that the particle–particle associations require higher energy to break and/or a faster rate of bond  
260 formation over shear-initiated breakage. These interactions are decided by the layer charge density  
261 and particle size of Sap. In this context, according to  $\sigma = EK(N^2/2)$  (where  $\sigma$  is shear stress,  $E$  is  
262 the energy of the bond,  $K$  is a rate constant for bond formation and breakage, and  $N$  is the number  
263 of particles per  $\text{cm}^3$  that are constantly forming and breaking bonds during the shear/flow  
264 process),<sup>44</sup> and provided that the bond energy between Sap particles and the rates at which bonds  
265 form and break are almost constant in the hydrogel of the Sap20 and the Sap25, the number of  
266 bonds forming and breaking will play a larger role in shear stress than that in the Sap10 and the  
267 Sap15. Since all dispersions were completed at the same solid concentration, any changes in the  
268 number of bonds forming or breaking can be attributed to differences in particle size (number of  
269 layers associated with each quasicrystal). The number of layers associated with each quasicrystal  
270 can be then related to layer charge as discussed above. Furthermore, as (plastic) viscosity is  
271 represented by the slope of the shear stress curve,  $\sigma = \sigma_e + \eta\Omega$  (where  $\sigma_e$  is the extrapolated shear  
272 stress,  $\eta$  is viscosity, and  $\Omega$  is the shear rate),<sup>45</sup> viscosity is also influenced strongly by  $N$ . It worth  
273 noting that at a shear rate of  $1.45 \text{ s}^{-1}$ , Sap20 and Sap25 followed a typical plastic flow, whereas  
274 dilatant flow behavior was observed for Sap10 and Sap15. The phenomena implied that, given the  
275 higher layer charges for Sap10 and Sap15 resulting in larger particles, above a threshold shear  
276 force, delamination of Sap particles occurred and thus increased swelling resulted in increased  
277 dispersion viscosity. Experimental results of shear rate versus shear stress can be fitted to the  
278 Herschel–Bulkley model.<sup>46</sup>  $\tau = \tau_0 + k\dot{\gamma}^n$ , where  $\tau_0$ ,  $k$ , and  $n$  are the Herschel–Bulkley yield  
279 stress, the consistency index, and the flow index parameters, respectively. The model also  
280 indicates that, under a certain shear force, delamination of Sap10 and Sap15 layers occurred and  
281 thus led to increased swelling when dispersed. The dispersion of Sap10 and Sap15 flowed because  
282 of their higher layer charge and larger particles. Regarding Sap20 and Sap25, both exhibited  
283 plastic or Bingham flowing behavior. A linear response above the critical shear rate means that the  
284 rate of energy dissipation per unit volume is at equilibrium with the rate of shear. By contrast, for  
285 Sap10 and Sap15 dispersions, only the rate of energy dissipation per unit volume is at equilibrium  
286 with a shear rate of  $1.45 \text{ s}^{-1}$ . Under a nonsteady state, the Sap hydrogels displayed thixotropy  
287 (Figure 2c), as the plots of shear stress versus shear rate exhibited characteristic hysteresis<sup>47</sup> and  
288 revealed that all Sap hydrogels are non-Newtonian fluids. Thixotropy is defined as the area within

289 the flow curve loop, increasing and then decreasing with the applied shear rate. Thixotropy values  
290 for Sap10 and Sap15 hydrogels were 4830 and 4643 Pa·s<sup>-1</sup>, whereas for Sap20 and Sap25  
291 hydrogels were 10573 and 7706 Pa·s<sup>-1</sup>, respectively, in the shear rate range of 1.45–1000 s<sup>-1</sup>.  
292 Sap20 had the largest thixotropic loop area and also displayed the highest shear stress. The larger  
293 area of the thixotropic loop for Sap20 and Sap25 hydrogels revealed that they exhibited a stronger  
294 thixotropy than Sap10 and Sap15 hydrogels. Such differences in thixotropy might be caused by  
295 the distinct particle associations in sample Sap20 as observed by SEM (Figure 7g). Theoretically,  
296 in the Sap gel, equilibrium is never achieved between the bond formation and bond breakage, as  
297 the Sap system undergoes shear. In regard to Sap10 and Sap15 hydrogels, the lack of oscillations  
298 indicates that equilibrium conditions are essentially met. Some further evidence of thixotropic  
299 behavior being affected by layer charge density and particle size (inherently particle associations  
300 and bonding) can be seen as oscillations in the shear responses within the hysteresis loops (Figure  
301 2d). The storage modulus ( $G'$ ) reflects the energy storage and elastic properties of the material  
302 after perturbation.<sup>48</sup> The loss modulus ( $G''$ ) reflects the energy loss and viscous properties of the  
303 material through the relaxation or dissipation of energy (usually as heat).<sup>49</sup> For the four samples,  
304 the  $G'$  exceeded the  $G''$  at a frequency ranging from 1 to 10 Hz at  $25 \pm 0.1$  °C and indicated that  
305 the Sap dispersions behave as hydrogels.<sup>50</sup> In other words, they tended to form bonds and  
306 decrease  $N$  over time. The hydrogel formed by the Sap20 possessed the highest  $G'$  and  $G''$ .  
307

### 308 **3.3 Crystallinity and morphology of Sap**

309 All of the Sap samples exhibited a plated morphological structure as observed in SEM images  
310 (Figure 7). For the SEM images of Sap5 (Figure S7), slices of curved plates with well-defined  
311 edges can be clearly observed, indicating that well-crystallized layered saponite was achieved.<sup>34</sup>  
312 Compared to Sap5, the Sap10 samples consist of smaller secondary and primary Sap particles  
313 (Figure 7a). Thus, incorporation of less Al into the Sap framework hampered the formation of  
314 large plates. This trend was more obvious for the Sap15 (Figure 7b). In particular, Sap20 (Figure  
315 7c) has a larger size than the other Sap, except for Sap5, possibly a result of distinct aggregation.  
316 This distinction has been found in the measurement of the thixotropic behavior of the gel from  
317 aqueous Sap20 dispersion (Figure 5). The SEM image of the Sap25 (Figure 7d) also showed a  
318 platy morphology. The results (Table 1) obtained from dynamic light scattering (DLS) also  
319 revealed that Sap20 behaved differently when compared with the others. The average particle  
320 sizes of Sap5, Sap10, Sap15, Sap20, and Sap25, as measured by DLS, were 502, 171, 148, 245,  
321 and 144 nm, respectively. Particle size decreased gradually with an increasing Si/Al molar ratio  
322 from 5 to 15 but increased by ca. 100 nm for Sap20. These results correlate well with SEM  
323 observations and rheology results. Moreover, the pore structure of Sap20 appeared different. The  
324 average pore diameters of Sap5, Sap10, Sap15, Sap20, and Sap25 were 3.61, 3.68, 3.34, 3.08, and  
325 3.16 nm, respectively (Figure S8). The Barrett–Joyner–Halenda desorption cumulative pore  
326 volumes of Sap5, Sap10, Sap15, Sap20, and Sap25 between 2.05 and 3.10 nm were 0.0122,  
327 0.0118, 0.0416, 0.0624, and 0.0490 cm<sup>3</sup>/g, respectively. The differences in particle size and pore

328 structure are related to the formed hydrogel. The hydrogel strength (shear pressure) is much  
329 stronger in Sap20 than the others. In Sap–water systems, an electronic double layer was made up  
330 of the negative surface charge and the balancing cation charge. As discussed above, for all Sap  
331 samples, the negative charge of the Sap layer is a consequence of isomorphous substitutions  
332 within the saponite crystal lattice. The counterions were electrostatically attracted by the  
333 oppositely charged surface (Figure 2e) but had a tendency to diffuse away from the surface to the  
334 bulk solution where its concentration is lower. The concentration of the counterions near the Sap  
335 particle surface was high, and it decreased with increasing distance away from the surface of the  
336 Sap particle. The diffuse layer did not only consist of an excess of opposite ions but also a  
337 deficiency of anions near the surface, as the ions with the same charge were electrostatically  
338 repelled by the surface of the Sap particle. Here, in the sap–water suspension system, the cations  
339 were adsorbed onto the surface of Sap particles and, together with the counterions, formed a  
340 diffuse double layer (Figure 2e). The higher charge potential at the Sap surface overrode the  
341 tendency for the cations to hydrate with water, so the charge was more effectively neutralized and  
342 the diffuse double layer contracted. As such, the (absolute value of)  $\zeta$ -potential of Sap dispersion  
343 also appeared to be higher for the Sap carrying a higher layer charge density (Figure 5a). The  
344 gel-forming ability of the dispersion of Sap in water was affected by both the layer charge density  
345 of Sap and the relevant associations and connections of Sap particles. For the lowest layer charge  
346 density, Sap can be more easily dispersed and delaminated in water to form a house-of-card  
347 structure. Such gels displayed higher viscosity and thixotropy, explaining why the Sap20 hydrogel  
348 exhibited the largest area of a thixotropic loop (Figure 2c) and the Sap25 hydrogel exhibited the  
349 highest viscosity. This implies that the thixotropic rheological properties of the Sap gel were  
350 closely related to the chemical composition of Sap and association modes between the Sap  
351 particles into water.  
352

### 353 **3.4 Rheological behavior affected by sodium polyacrylate**

354  
355 For the purpose of tuning the shear thinning of Sap hydrogels and studying the influence of the  
356 NaPA on the different Sap hydrogels, NaPA with concentrations of 0.1, 0.19, 0.28, 0.36, and 0.44  
357 g/L was loaded into the Sap hydrogels. The infinite viscosity of the Sap-NaPA dispersions tends to  
358 zero. This phenomenon indicated that the addition of NaPA induced shear thinning (Figure 3a–d).  
359 In regard to Sap-NaPA0.1 dispersions made from Sap10, Sap15, Sap20, and Sap25 hydrogels with  
360 added NaPA at a concentration of 0.1 g/L, the viscosity decreased rapidly as the shear rate  
361 increased from 0 to 2.5 s<sup>-1</sup>. Comparing the Sap10-NaPA0.1 dispersion to dispersions of  
362 Sap15-NaPA0.1, Sap20-NaPA0.1, and Sap25-NaPA0.1, the decline in viscosity was much slower  
363 and may be due to the higher layer charge density of Sap10 (0.74 e/pfu). For all SapNaPA  
364 dispersions, as the shear rate increased from 2.5 to 10 s<sup>-1</sup>, the viscosity declined slowly. When  
365 the shear rate increased to more than 10 s<sup>-1</sup>, all Sap-NaPA dispersions were similar to liquids  
366 with very low viscosity, especially at the equilibrium viscosity. The result suggested that the effect  
367 of NaPA on Sap hydrogels was less significant at very high mechanical forces and the addition of

368 NaPA weakened the particle-to-particle connections between Sap particles in hydrogels.  
369 Furthermore, the Sap dispersions in the presence of NaPA are well fitted with the Sisko model  
370 (Figure S2a–d). The infinite viscosity of the Sap-NaPA dispersions tends to zero, indicating that  
371 the addition of NaPA induced shear thinning. Shear stress as a function of shear rate for different  
372 SapNaPA dispersions is shown in Figure 4. The results of shear stress versus shear rate showed  
373 that the Sap-NaPA dispersion followed a plastic flow and fit the Herschel–Bulkley  $\tau = \tau_0 + k\dot{\gamma}^n$   
374 model<sup>46</sup> (Figure S3a–d). The shear stress of all Sap-NaPA dispersions decreased with the increase  
375 of the concentration of the NaPA (Figure 4a–d). In addition, it was noted that the shear stress  
376 increased with increasing shear rate, except for Sap10-NaPA0.1, in which the shear rate had an  
377 indistinctive influence on shear stress (Figure S3a). The reason is that the layer charge density of  
378 Sap10 (0.74 e/pfu) is higher than the others. The low concentration (0.1 g/L) of NaPA had an  
379 insignificant influence on the hydrogel formation for Sap10.

380 Without adding NaPA in Sap hydrogels, the yield stresses ( $\tau_0$ ) of Sap10 and Sap15 were 13.35 and  
381 14.93 Pa, respectively, whereas they were 29.33 and 66.17 Pa for Sap20 and Sap25, respectively.  
382 When the concentration of added NaPA was 0.1 g/L, the yield stresses ( $\tau_0$ ) of Sap10-NaPA0.1 and  
383 Sap15-NaPA0.1 were 7.09 and 7.38 Pa, respectively, whereas they were 13.32 and 25.65 Pa for  
384 Sap20-NaPA0.1 and Sap25-NaPA0.1, respectively. With an increased NaPA concentration, the  
385 yield stress  $\tau_0$  decreased gradually and tended toward zero, indicating that the Sap hydrogel  
386 tended to be sol when NaPA was added. The Sap20 and Sap25, with a lower layer charge density  
387 than Sap10 and Sap15, were more difficult to flow for their hydrogels and dispersions with  
388 addition of NaPA. The thixotropic behavior of Sap dispersions was also affected by NaPA. For all  
389 Sap-NaPA dispersions, the dispersions are still thixotropic (Figure S4a–d). NaPA concentration  
390 had no observable effect on the area of the thixotropic loop for Sap20- NaPa, but the areas of the  
391 Sap20-NaPA complexes were reduced significantly compared to that of the Sap20 hydrogel. The  
392 same phenomenon was observed for Sap25-NaPA dispersion. Such results in thixotropy suggested  
393 that the concentrations of NaPA had an indistinctive influence on thixotropy for Sap20 and Sap25  
394 hydrogels. The shear thinning and thixotropy of Sap dispersions derived from the characteristics  
395 of the network formed by Sap particles; the network was destroyed as the shear rate increased. In  
396 contrast, when the shear rate decreased, the aggregation of Sap layers could be rebuilt to be a  
397 whole network. The frequency response of the  $G'$  and the  $G''$  of the Sap dispersions in the  
398 presence of NaPA is shown in Figure S5a–d.

399 For all Sap-NaPA dispersions, as the frequency increased,  $G'$  was first lower than  $G''$  and then  $G'$   
400 became higher than  $G''$ . Compared to Sap dispersions without the addition of NaPA, the  $G'$  at the  
401 analyzed frequencies decreased by several orders of magnitude and the  $G''$  was higher than the  $G'$   
402 at lower frequencies. In other words, adding NaPA in the Sap dispersion led to a viscoelastic  
403 liquidlike sol.<sup>51</sup> This sol was not a pure viscous fluid at the analyzed frequencies. The elastic  
404 component of the viscoelastic sol indicated a tendency to gel.<sup>52</sup> Based on the discussion of the  
405 above results, it can be concluded that the addition of NaPA induced changes in the rheological

406 properties of Sap hydrogels. After adding NaPA into the Sap hydrogel system, the Sap hydrogels  
407 transformed to sols by weakening the connections between Sap particles, resulting in a decrease in  
408 the viscosity and thixotropy of Sap dispersions.

409

### 410 **3.5 Interaction between the anionic polyelectrolyte and Sap**

411 The  $\zeta$ -potential of 1.5 wt % Sap dispersions was plotted as a function of NaPA concentration  
412 (Figure 5a). The  $\zeta$ potential of all Sap samples is less than  $-38$  mV. Sap with a higher layer charge  
413 displayed a higher  $\zeta$ -potential. At a given NaPA concentration, the  $\zeta$ -potential of Sap10 (0.74 e/pfu)  
414 was the highest compared to the other Sap samples. The  $\zeta$ potential of the Sap represented the  
415 change in the layer charge of the particles as a function of their composition. Over the entire range  
416 of NaPA concentrations, the  $\zeta$ -potential values indicated a strong negative charge on the surface of  
417 Sap particles. The  $\zeta$ -potential of negative charge increased significantly as the NaPA gradually  
418 covered the surface of the particles. Thus, NaPA increased electrostatic repulsion between Sap  
419 particles and promoted the stabilization of Sap dispersion.<sup>53</sup> The rheological properties of Sap  
420 with addition of NaPA changed, which can be described as the Hofmeister effect.<sup>54</sup> The FTIR  
421 spectra of the dried samples, which were made from the Sap dispersions with an added 0.44 g/L  
422 NaPA, are similar to those of the samples without added NaPA (Figure S6), except that the  
423 presence of NaPA could be observed in the Sap25-NaPA0.44 sample (Figure S6d). The bonds at  
424  $1559$  and  $1325$   $\text{cm}^{-1}$  are ascribed to the symmetrical stretching vibrations of  $\text{COO}^-$ . The bond at  
425  $1407$   $\text{cm}^{-1}$  is due to the  $\text{C}=\text{O}$  bending in carboxylate groups. Those bonds were also detected in  
426 Sap25-NaPA0.44. Notably, no change in the vibration bands could be observed, revealing that the  
427 addition of NaPA did not generate new chemical bonds. The presence of NaPA in the  
428 Sap25-NaPA0.44 is probably the adsorption of NaPA on the surfaces of Sap25 by electrostatic  
429 attraction and hydrogen bonding. To better illustrate the interaction between NaPA and Sap, a  
430 possible schematic illustration is proposed (Figure 5). NaPA has a carboxylate functional group,  
431 which ionizes in water (Figure 5bI); thus, it can be dissociated to form  $\text{PA}^-$ . Due to the surface  
432 charge in the vicinity of the Sap particle, an electric field strength formed.<sup>55</sup> Under such an  
433 electric field, the negatively charged  $\text{PA}^-$  underwent an instantaneous polarization,<sup>56</sup> which can  
434 enter into the Sap hydration sphere faster than the original hydrated ions.  $\text{PA}^-$  would  
435 electrostatically interact with the exchange cations as  $\text{PA}^-$  and can approach closer to the cations  
436 than the cations to the surface of the clay (due to water).  $\text{PA}^-$  displaced water and formed a strong  
437 bond because of the stronger electrostatic attraction. At these very low NaPA concentrations, the  
438  $\text{PA}^-$  interacts with the exterior surfaces of the Sap quasicrystals but eventually by mass action  
439 enables delamination. Consequently, after adding NaPA into the Sap hydrogel, the Sap hydrogel  
440 transformed into a Sap dispersion resulting from the destruction of the original network structure  
441 (Figure 5bII). The destruction of the network structure can be ascribed to the electrostatic  
442 attraction between polarized  $\text{PA}^-$  and negatively charged Sap particles and possible hydrogen

443 bonding between broken bonds, Mg–O and Si–O, at the edges of tetrahedral/octahedral sheets of  
444 Sap and hydrogen atoms on PA<sup>-</sup>. Another possible reason is when NaPA was introduced into the  
445 Sap hydrogel system, the width of the diffuse layer increased because PA<sup>-</sup> has a larger molecular  
446 size than original hydrate ions. Additionally, to further investigate the interaction between Sap and  
447 NaPA, powder XRD and SEM were carried out for Sap-control (dried from the Sap hydrogel) and  
448 Sap-NaPA (dried from the Sap hydrogel after adding NaPA). Comparing XRD pattern of  
449 Sap10-NaPA0.44 (dried from Sap10 dispersions, after adding NaPA at the concentration of 0.44  
450 g/L) with that of the Sap10-control, the intensity of the (001) reflection increased and the full  
451 widths at half-maximum (FWHM) significantly decreased for Sap10-NaPA0.44 samples (Figure  
452 6a). Such results can indicate that the addition of NaPA induced a better coherency in the c  
453 dimension for Sap10 layers, i.e., a higher number of Sap layers stacked. Regarding the other  
454 SapNaPA0.44 (dried from Sap<sub>x</sub> dispersions, where x is 15, 20, or 25 mole% Al in Sap, after  
455 adding NaPA at the concentration of 0.44 g/L), the intensity of the (001) reflection increased but  
456 the FWHM significantly increased when compared with their corresponding Sap-control (Figure  
457 6b–d). The results indicate that PA<sup>-</sup> was able to penetrate the interlayer, resulting in delamination.  
458 The SEM observations of Sap-NaPA0.44 revealed that these Sap samples have a more compact  
459 and ordered layer structure than the raw Sap (Figure 7). Sap in the water system dispersed and  
460 formed hydrogels after standing for 7 d and dried from dispersions reassembled in the first  
461 instance (Figure 7e–h). A schematic illustration of Sap dispersion with/without added NaPA and  
462 reaggregation after drying is presented in Figure 5c to clarify the interaction process between Sap,  
463 water, and NaPA. After adding NaPA into the Sap hydrogel, the house-of-card structure was  
464 destroyed and the Sap hydrogel became more dispersed (Figure 5cVI). When the Sap-NaPA0.44  
465 dispersion was dried, the dispersed Sap particles reassembled in a more ordered, regular, and  
466 compact structure (Figure 5cVII). Interestingly, as seen in Figure 7g, Sap20-NaPA0.44 exhibited  
467 the best compact structure among the Sap-NaPA0.44 samples, suggesting that the  
468 reassembly/reaggregation of negatively charged Sap layers reacted with polarized PA<sup>-</sup>, which  
469 may be caused by the strength of the Sap layer charge density. The Sap20 with the layer charge  
470 density of 0.42 e/pfu delaminated best in a water/NaPA system and reassembled/ reaggregated  
471 better than the other Sap with unmatched layer charge density. Such results further confirmed that  
472 the NaPA not only affected the rheological properties of Sap dispersion but also promoted the  
473 reassembled Sap to form a superior crystal structure by interacting with the Sap hydration sphere  
474 in Sap dispersion.

475

#### 476 **4. Conclusion**

477 Saponites, with a Si/Al molar ratio ranging from 5 to 25, were successfully synthesized by a  
478 simple hydrothermal process. The Si/Al molar ratio had a remarkable influence on the crystallinity,

479 morphology, and particle size of the synthetic Sap. The lowest Si/Al molar ratio (5) led to  
480 improved Sap crystallinity. However, for this lowest ratio, the synthetic Sap did not delaminate  
481 easily, probably due to a high layer charge, and was unable to form gel in aqueous dispersion. On  
482 the other hand, the aqueous dispersions (3 wt %) of synthetic Sap, with a Si/Al molar ratio ranging  
483 from 10 to 25, formed gel spontaneously. The Sap hydrogel had remarkable rheological properties  
484 that were related to the chemical composition and inherently to its crystallinity, layer charge, and  
485 particle size. The hydrogel from the Sap with a Si/Al molar ratio of 25 exhibited the highest  
486 viscosity, which was ascribed to better delamination and the formation of an open house-of-card  
487 structure with stronger connections of delaminated Sap particles compared to the other synthetic  
488 Sap. The addition of the anionic polyelectrolyte NaPA decreased the viscosity and reduced the  
489 thixotropic properties of the Sap hydrogel. Moreover, the addition of NaPA caused the hydrogel to  
490 become sol. The aqueous dispersion of the Sap with NaPA formed a stable sol, compared to the  
491 Sap sol or Sap hydrogel. The colloidal stabilization of Sap by NaPA is considered to be due to the  
492 Hofmeister effect. In the hydrogel, electrostatic interactions between synthetic Sap particles and  
493 NaPA occurred. The anionic NaPA could be instantaneously polarized under the electric field of  
494 Sap particles and, as a result, quickly entered the hydration layer of Sap particles to disrupt the  
495 structure of Sap gel, thereby changing the Sap dispersion in water. Such effects of sodium  
496 polyacrylate can be further investigated to finely tune the rheological behaviors of synthetic  
497 saponite hydrogels and can be used to exfoliate swelling clay minerals into 2D nanosheets.

498

499

500

## 501 **Acknowledgments**

502 The authors wish to acknowledge the financial support from the National Natural Scientific Foundation of China (41672033;  
503 21373185), the financial support by the open fund from Key Laboratory of High Efficient Processing of Bamboo of Zhejiang Province,  
504 China National Bamboo Research Center,,Key Laboratory of Clay Minerals of Ministry of Land and Resources of the People's Republic  
505 of China, Engineering Research Center of Non-metallic Minerals of Zhejiang Province, Zhejiang Institute of Geology and Mineral  
506 Resource, China (ZD2018K05), and the State Key Laboratory Breeding Base of Green Chemistry-Preparation Technology, Zhejiang  
507 University of Technology (GCTKF2014006).

508

- 509 (1) Newman, A.C.D.; Brown, G. The Chemical Composition of Clays. In Chemistry of Clays  
510 and Clay Minerals; Newman, A.C.D., Ed.; The Mineralogical Society: London, 1987; Chapter 1,  
511 Vol. p1-128, pp 480.
- 512 (2) Bergaya, F.; Lagaly, G. Chapter 1 - General Introduction: Clays, Clay Minerals, and Clay  
513 Science. In Developments in Clay Science, Second Edition. Handbook of Clay Science; Bergaya,  
514 F.; Bergaya, F.; Lagaly, G., Eds.; Elsevier, 2013; Vol. 1, pp 1–19.
- 515 (3) Tao, Q.; Fang, Y.; Li, T.; Zhang, D.; Chen, M.; Ji, S.; He, H.; Komarneni, S.; Zhang, H.;  
516 Dong, Y.; Noh, Y. D. Silylation of saponite with 3-aminopropyltriethoxysilane. *Appl. Clay Sci.*  
517 2016, 132–133, 133–139.
- 518 (4) Takagi, S.; Shimada, T.; Ishida, Y.; Fujimura, T.; Masui, D.; Tachibana, H.; Eguchi, M.;  
519 Inoue, H. Size-Matching Effect on Inorganic Nanosheets: Control of Distance, Alignment, and  
520 Orientation of Molecular Adsorption as a Bottom-Up Methodology for Nanomaterials.  
521 *Langmuir* 2013, 29, 2108–2119.
- 522 (5) Huang, J.; Wang, L.; Li, T.; Shao, J. Rheological studies of mineral clay and its application  
523 in reactive dye printing of cotton. *Text. Res. J.* 2017, 88, 614–620.
- 524 (6) Zhen, W.; Lu, C.; Li, C.; Liang, M. Structure and properties of thermoplastic  
525 saponite/poly(vinyl alcohol) nanocomposites. *Appl. Clay Sci.* 2012, 57, 64–70.
- 526 (7) Bernardini, F.; Sibilina, E.; Kasztovszky, Z.; Boscutti, F.; De Min, A.; Lenaz, D.; Turco, G.;  
527 Micheli, R.; Tuniz, C.; Montagnari Kokelj, M. Evidence of open-air late prehistoric occupation in  
528 the Trieste area (north-eastern Italy): dating, 3D clay plaster characterization and obsidian  
529 provenancing. *Archaeol. Anthropol. Sci.* 2018, 10, 1933–1943.
- 530 (8) Dazas, B.; Lanson, B.; Delville, A.; Robert, J.-L.; Komarneni, S.; Michot, L. J.; Ferrage, E.  
531 Influence of tetrahedral layer charge on the organization of interlayer water and ions in synthetic  
532 Na-saturated smectites. *J. Phys. Chem. C* 2015, 119, 4158–4172.
- 533 (9) Bergaya, F.; Lagaly, G. Chapter 7.1 - Purification of Natural Clays. In Developments in Clay  
534 Science Edition. 2nd Edition Handbook of Clay Science; Bergaya, F.; Lagaly, G., Eds.; Elsevier:  
535 Amsterdam, 2013; Vol. 5, pp 213–221.
- 536 (10) Gebretsadik, F. B.; Mance, D.; Baldus, M.; Salagre, P.; Cesteros, Y. Microwave synthesis  
537 of delaminated acid saponites using quaternary ammonium salt or polymer as template. Study of  
538 pH influence. *Appl. Clay Sci.* 2015, 114, 20–30.
- 539 (11) Garciano, L. O.; Tran, N. H.; Kannangara, G. S. K.; Milev, A. S.; Wilson, M. A.; Volk, H.  
540 Developing saponite supported cobalt– molybdenum catalysts for upgrading squalene, a  
541 hydrocarbon from the microalgae *Botryococcus braunii*. *Chem. Eng. Sci.* 2014, 107, 302–310.
- 542 (12) Vogels, R. J. M. J.; Kloprogge, J. T.; Geus, J. W. Synthesis and characterization of saponite  
543 clays. *Am. Mineral.* 2005, 90, 931–944.
- 544 (13) Intachai, S.; Khaorapong, N.; Ogawa, M. Hydrothermal synthesis of zinc selenide in  
545 smectites. *Appl. Clay Sci.* 2017, 135, 45– 51.
- 546 (14) Suquet, H.; Iiyama, J. T.; Kodama, H.; Pezerat, H. Synthesis and Swelling Properties of  
547 Saponites with Increasing Layer Charge. *Clays Clay Miner.* 1977, 25, 231–242.
- 548 (15) Gebretsadik, F. B.; Salagre, P.; Cesteros, Y. Use of polymer as template in microwave  
549 synthesis of saponite. Study of several factors of influence. *Appl. Clay Sci.* 2014, 87, 170–178.
- 550 (16) Bergada, O.; Vicente, I.; Salagre, P.; Cesteros, Y.; Medina, F.; Sueiras, J. E. Microwave effect  
551 during aging on the porosity and basic properties of hydrotalcites. *Microporous Mesoporous Mater.*  
552 2007, 101, 363–373.



553 (17) Vogels, R. J. M. J.; Kerkhoffs, M. J. H. V.; Geus, J. W. Nonhydrothermal Synthesis,  
554 Characterisation and Catalytic Properties of Saponite Clays. In *Studies in Surface Science and*  
555 *Catalysis*; Poncelet, G.; Martens, J.; Delmon, B.; Jacobs, P. A.; Grange, P., Eds.; Elsevier, 1995;  
556 Vol. 91, pp 1153–1161.

557 (18) Zhou, C. H.; Zhou, Q.; Wu, Q. Q.; Petit, S.; Jiang, X. C.; Xia, S. T.; Li, C. S.; Yu, W. H.  
558 Modification, hybridization and applications of saponite: An overview. *Appl. Clay Sci.* 2019, 168,  
559 136–154.

560 (19) Makarchuk, O. V.; Dontsova, T. A.; Astrelin, I. M. Magnetic nanocomposites as efficient  
561 sorption materials for removing dyes from aqueous solutions. *Nanoscale Res. Lett.* 2016, 11, No.  
562 161.

563 (20) Chen, L.; Zhou, C. H.; Fiore, S.; Tong, D. S.; Zhang, H.; Li, C. S.; Ji, S. F.; Yu, W. H.  
564 Functional magnetic nanoparticle/clay mineral nanocomposites: preparation, magnetism and  
565 versatile applications. *Appl. Clay Sci.* 2016, 127–128, 143–163.

566 (21) Annan, E.; Kan-Dapaah, K.; Azeko Salifu, T.; Mustapha, K.; Asare, J.; Zebaze Kana, M. G.;  
567 Soboyejo, W. Clay mixtures and the mechanical properties of microporous and nanoporous  
568 ceramic water filters. *J. Mater. Civ. Eng.* 2016, 28, No. 04016105.

569 (22) Tao, Q.; Chen, M.; He, H.; Komarneni, S. Hydrothermal transformation of mixed metal  
570 oxides and silicate anions to phyllosilicate under highly alkaline conditions. *Appl. Clay Sci.* 2018,  
571 156, 224–230.

572 (23) Tombacz, E.; Szekeres, M. Colloidal behavior of aqueous montmorillonite suspensions: the  
573 specific role of pH in the presence of indifferent electrolytes. *Appl. Clay Sci.* 2004, 27, 75–94. (24)  
574 Grandjean, J.; Robert, J.-L. Multinuclear magnetic resonance studies on aqueous suspensions of  
575 synthetic saponites. *J. Colloid Interface Sci.* 1997, 187, 267–273.

576 (25) Gao, X.; Li, S.; Liu, X.; Hu, F.; Tian, R.; Li, H. The effects of NO<sub>3</sub><sup>-</sup> and Cl<sup>-</sup> on negatively  
577 charged clay aggregation. *Soil Tillage Res.* 2019, 186, 242–248.

578 (26) GÜNGÖR, N. Effect of the adsorption of surfactants on the rheology of Na-bentonite slurries. *J.*  
579 *Appl. Polym. Sci.* 2000, 75, 107– 110.

580 (27) Shaikh, S. M.; Nasser, M. S.; Hussein, I.; Benamor, A.; Onaizi, S. A.; Qiblawey, H. Influence  
581 of polyelectrolytes and other polymer complexes on the flocculation and rheological behaviors of  
582 clay minerals: A comprehensive review. *Sep. Purif. Technol.* 2017, 187, 137–161.

583 (28) Tong, K.; Song, X.; Sun, S.; Xu, Y.; Yu, J. The rheological behavior and stability of Mg(OH)<sub>2</sub>  
584 aqueous suspensions in the presence of sodium polyacrylate. *Colloids Surf., A* 2013, 436, 1111–  
585 1120.

586 (29) Fu, L.-h.; Cao, T.-h.; Lei, Z.-w.; Chen, H.; Shi, Y.-g.; Xu, C. Superabsorbent nanocomposite  
587 based on methyl acrylic acid-modified bentonite and sodium polyacrylate: Fabrication, structure  
588 and water uptake. *Mater. Des.* 2016, 94, 322–329.

589 (30) Kaufhold, S.; Plötze, M.; Klinkenberg, M.; Dohrmann, R. Density and porosity of bentonites.  
590 *J. Porous Mater.* 2013, 20, 191– 208.

591 (31) Wang, W.; Zhen, W.; Bian, S.; Xi, X. Structure and properties of quaternary fulvic  
592 acid–intercalated saponite/poly(lactic acid) nanocomposites. *Appl. Clay Sci.* 2015, 109–110,  
593 136–142.

594 (32) Chemtob, S. M.; Nickerson, R. D.; Morris, R. V.; Agresti, D. G.; Catalano, J. G. Synthesis  
595 and structural characterization of ferrous trioctahedral smectites: Implications for clay mineral  
596 genesis and detectability on Mars. *J. Geophys. Res.: Planets* 2015, 120, 1119–1140.

597 (33) Brown, G.; Brindley, G. W. Chapter 5 - X-ray Diffraction Procedures for Clay Mineral  
598 Identification. In Mineralogical Society Monograph; Brindley, G.; Brown, G., Eds.; Mineralogical  
599 Society: London, 1980; Vol. 5, pp 305–359.

600 (34) Rajapakse, R.; Murakami, K.; Bandara, H.; Rajapakse, R.; Velauthamurti, K.; Wijeratne, S.  
601 Preparation and characterization of electronically conducting polypyrrole-montmorillonite  
602 nanocomposite and its potential application as a cathode material for oxygen reduction.  
603 *Electrochim. Acta* 2010, 55, 2490–2497.

604 (35) He, H.; Li, T.; Tao, Q.; Chen, T.; Zhang, D.; Zhu, J.; Yuan, P.; Zhu, R. Aluminum ion  
605 occupancy in the structure of synthetic saponites: Effect on crystallinity. *Am. Mineral.* 2014, 99,  
606 109–116.

607 (36) Madejova, J.; Gates, W. P.; Petit, S. Chapter 5 - IR Spectra of Clay Minerals Developments  
608 in Clay Science, Infrared and Raman Spectroscopies of Clay Minerals; Gates, W. P.; Kloprogge, J.  
609 T.; Madejova, J.; Bergaya, F., Eds.; Elsevier: Amsterdam, 2017; Vol. 8, pp 107–149.

610 (37) Madejova, J. FTIR techniques in clay mineral studies. *Vib. Spectrosc.* 2003, 31, 1–10.

611 (38) Petit, S.; Baron, F.; Decarreau, A. Synthesis of nontronite and other Fe-rich smectites: a  
612 critical review. *Clay Miner.* 2017, 52, 469– 483.

613 (39) Philippe, A.; Baravian, C.; Bezuglyy, V.; Angilella, J.; Meneau, F.; Bihannic, I.; Michot, L.  
614 Rheological study of two-dimensional very anisometric colloidal particle suspensions: from  
615 shear-induced orientation to viscous dissipation. *Langmuir* 2013, 29, 5315–5324.

616 (40) Suquet, H.; Pezerat, H. Parameters influencing layer stacking types in saponite and  
617 vermiculite: A review. *Clays Clay Miner.* 1987, 35, 353–362.

618 (41) Chemedá, Y. C.; Christidis, G. E.; Khan, N. T.; Koutsopoulou, E.; Hatzistamou, V.; Kelessidis,  
619 V. C. Rheological properties of palygorskite–bentonite and sepiolite–bentonite mixed clay  
620 suspensions. *Appl. Clay Sci.* 2014, 90, 165–174.

621 (42) Soomro, F. A.; Usman, M.; Haq, R. U.; Wang, W. Melting heat transfer analysis of Sisko fluid  
622 over a moving surface with nonlinear thermal radiation via collocation method. *Int. J. Heat Mass*  
623 *Transfer* 2018, 126, 1034–1042.

624 (43) Rashidi, M.; Bagheri, S.; Momoniat, E.; Freidoonimehr, N. Entropy analysis of convective  
625 MHD flow of third grade non-Newtonian fluid over a stretching sheet. *Ain Shams Eng. J.* 2017, 8,  
626 77–85.

627 (44) Low, P. Interparticle forces in clay suspensions: flocculation, viscous flow and  
628 swelling. In *Clay Water Interface and its Rheological Implications*; Güven, N.; Pollastro, R. M.,  
629 Eds.; CMS Workshop Lectures: Boulder, 1992; Vol. 4, pp 157–190.

629 (45) Barnes, H. A.; Hutton, J. F.; Walters, K. F. R. S. Chapter 2- Viscosity. In *An Introduction to*  
630 *Rheology*; Barnes, H. A.; Hutton, J. F.; Walters, K. F. R. S., Eds.; Elsevier: Netherlands, 1993; Vol.  
631 3, pp 11– 36.

632 (46) Liu, R.; Ding, Z.; Hu, K. Stabilities in plane Poiseuille flow of Herschel–Bulkley fluid. *J.*  
633 *Non-Newtonian Fluid Mech.* 2018, 251, 132–144.

634 (47) Jeong, S. W.; Locat, J.; Torrance, J. K.; Leroueil, S. Thixotropic and anti-thixotropic  
635 behaviors of fine-grained soils in various flocculated systems. *Eng. Geol.* 2015, 196, 119–125.

636 (48) Gao, B.; Wang, X.-M.; Zhao, X.-Y.; Ding, X.; Fu, X.-X.; Zhang, Y.-L.; He, Q.-F.; Zhang, Z.;  
637 Liu, T.-Y.; Huang, Z.-Z.; Chen, L. G.; Peng, Y.; Guo, H. Source apportionment of atmospheric  
638 PAHs and their toxicity using PMF: impact of gas/particle partitioning. *Atmos. Environ.* 2015, 103,  
639 114–120.

640 (49) Zhang, X.; Xu, J.; Lang, C.; Qiao, S.; An, G.; Fan, X.; Zhao, L.; Hou, C.; Liu, J.  
641 Enzyme-regulated fast self-healing of a pillararenebased hydrogel. *Biomacromolecules* 2017, 18,  
642 1885–1892.

643 (50) Zamora-Mora, V.; Fernandez-Gutiérrez, M.; San Román, J.; Goya, G.; Hernandez, R.;  
644 Mijangos, C. Magnetic core–shell chitosan nanoparticles: Rheological characterization and  
645 hyperthermia application. *Carbohydr. Polym.* 2014, 102, 691–698.

646 (51) Kajiya, T.; Daerr, A.; Narita, T.; Royon, L.; Lequeux, F.; Limat, L. Advancing liquid contact  
647 line on visco-elastic gel substrates: stickslip vs. continuous motions. *Soft Matter* 2013, 9,  
648 454–461.

649 (52) Le Goff, K. J.; Gaillard, C.; Helbert, W.; Garnier, C.; Aubry, T. Rheological study of  
650 reinforcement of agarose hydrogels by cellulose nanowhiskers. *Carbohydr. Polym.* 2015, 116,  
651 117–123.

652 (53) Hasan, A.; Fatehi, P. Cationic kraft lignin-acrylamide copolymer as a flocculant for clay  
653 suspensions:(2) Charge density effect. *Sep. Purif. Technol.* 2019, 210, 963–972.

654 (54) Kunz, W.; Nostro, P. L.; Ninham, B. W. The present state of affairs with Hofmeister effects.  
655 *Curr. Opin. Colloid Interface Sci.* 2004, 9, 1–18.

656 (55) Gong, Y.; Tian, R.; Li, H. Coupling effects of surface charges, adsorbed counterions and  
657 particle-size distribution on soil water infiltration and transport. *Eur. J. Soil Sci.* 2018, 69,  
658 1008–1017.

659 (56) Del Gaudio, V.; Luo, Y.; Wang, Y.; Wasowski, J. Using ambient noise to characterise seismic  
660 slope response: The case of Qiaozhuang peri-urban hillslopes (Sichuan, China). *Eng. Geol.* 2018,  
661 246, 374–390.

662

**Table 1. Composition,  $\zeta$ -Potential, and Average Size of Sap, and Transparency of Sap Sol or Hydrogels**

sample <sup>a</sup>	theoretical molar ratio of Si/Mg/Al	theoretical LCD	actual molar ratio of Si/Mg/Al	actual LCD <sup>b</sup>	$\zeta$ (mV)	average size (nm)	transparency <sup>c</sup>
Sap <sub>5</sub>	6.6:6.0:1.3	1.33	6.0:6.0:1.2	1.33	-46.2	502	opaque
Sap <sub>10</sub>	7.3:6.0:0.7	0.73	6.4:6.0:0.7	0.74	-44.6	171	transparent
Sap <sub>15</sub>	7.6:6.0:0.5	0.50	6.5:6.0:0.5	0.53	-40.8	148	transparent
Sap <sub>20</sub>	7.6:6.0:0.4	0.38	6.7:6.0:0.4	0.42	-39.7	245	transparent
Sap <sub>25</sub>	7.7:6.0:0.3	0.31	6.7:6.0:0.3	0.35	-38.0	144	transparent

<sup>a</sup>Sap<sub>x</sub> indicates the Sap synthesized at the Si/Al molar ratio of x. <sup>b</sup>Data calculated according to the XRF analysis of Sap. In this work, the general formula of Sap can be written as (Na, Mg)<sub>x</sub>[Mg<sub>6</sub>][Si<sub>8-x</sub>Al<sub>x</sub>]O<sub>20</sub>(OH)<sub>4</sub>·nH<sub>2</sub>O with a charge x of 1.33–0.35 per O<sub>20</sub>(OH)<sub>4</sub>. <sup>c</sup>The transparency of these Sap samples is shown in Figure S1a(1). LCD: Layer charge density (e/per formula unit);  $\zeta$ : zeta-potential.

663

664

665

666

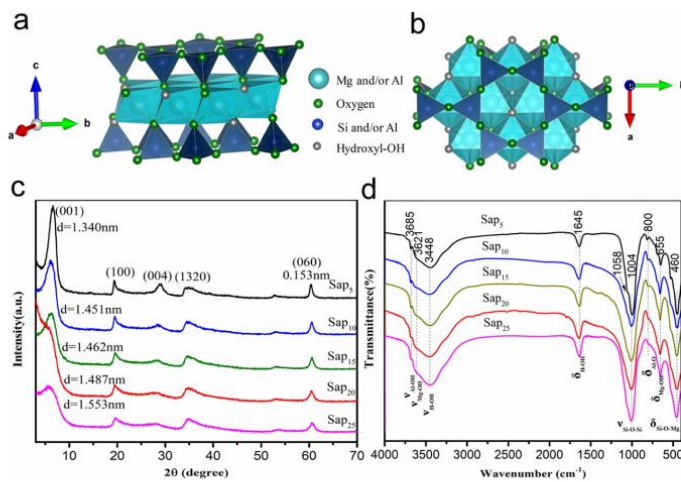


**Figure 1.** Crystal structure of Sap: (a) two tetrahedral sheets on each side of an octahedral sheet occupied by magnesium and/or aluminum cations, forming two-dimensional (2D) layers; (b) top view of Sap with trioctahedral. (c) Powder XRD patterns and (d) FTIR spectra of Sap<sub>x</sub>. Sap<sub>x</sub> indicates that the Sap was synthesized at the Si/Al molar ratio of x.

667

668

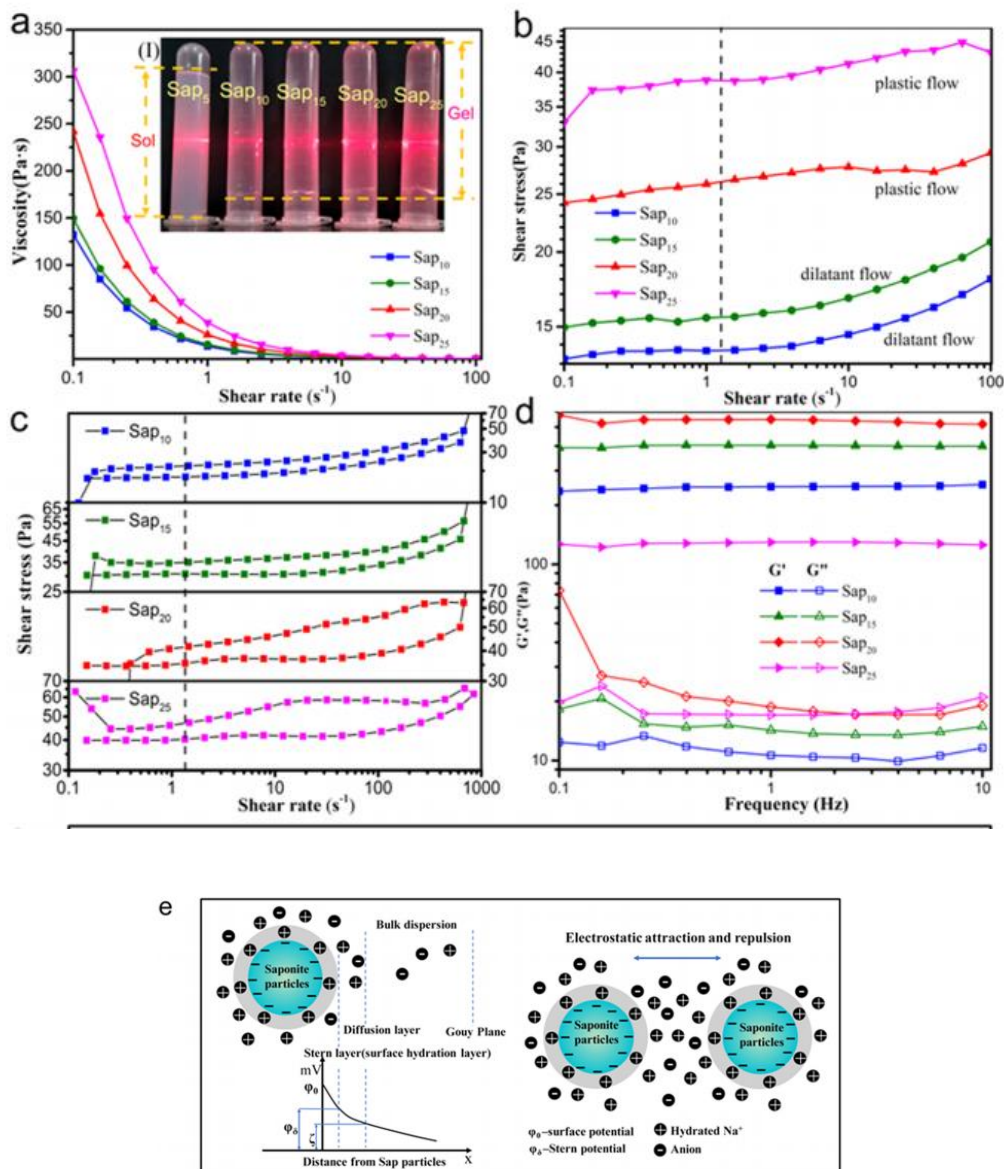


**Figure 2.** (a) Viscosity as a function of shear rate for Sap<sub>x</sub> hydrogels. (b) Shear stress as a function of shear rate for Sap<sub>x</sub> hydrogels (in the log–log mode). (c) Thixotropic loops as a function of shear rate for Sap<sub>x</sub> hydrogels (in the log–log mode). (d) Storage modulus ( $G'$ ) and loss modulus ( $G''$ ) of Sap<sub>x</sub> hydrogels (in the log–log mode). Schematic drawing of the dispersion mechanism for Sap particles: (e)  $\zeta$ -Potential of Sap and electrostatic force between Sap particles. The inset (I) in (a): the Tyndall effect (red laser beam) of Sap<sub>x</sub> hydrogels. Sap<sub>x</sub> means the Sap synthesized at the Si/Al molar ratios of 10, 15, 20, and 25.

669

670

671

672

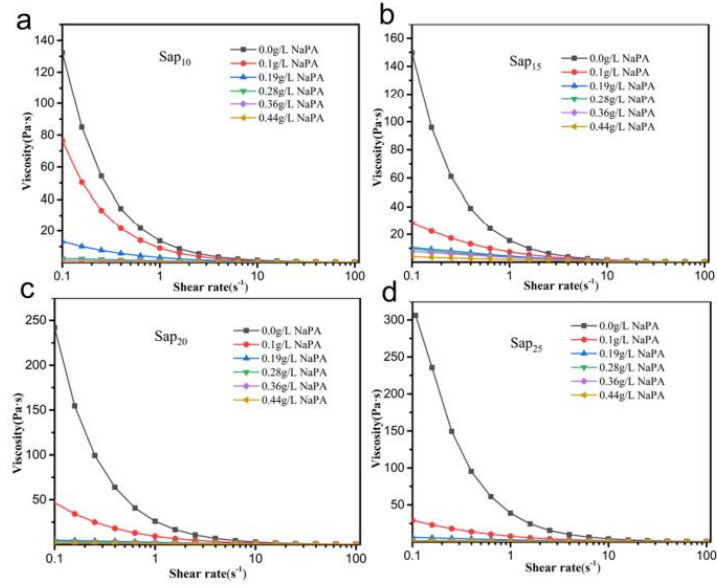


Figure 3. Viscosity as a function of shear rate (shear rate in the log mode) for (a) Sap<sub>10</sub>-NaPA <sub>$\gamma$</sub> , (b) Sap<sub>15</sub>-NaPA <sub>$\gamma$</sub> , (c) Sap<sub>20</sub>-NaPA <sub>$\gamma$</sub> , and (d) Sap<sub>25</sub>-NaPA <sub>$\gamma$</sub>  dispersions, where  $\gamma$  means the addition of NaPA from 0.1 to 0.44 g/L of aqueous Sap dispersion.

673

674

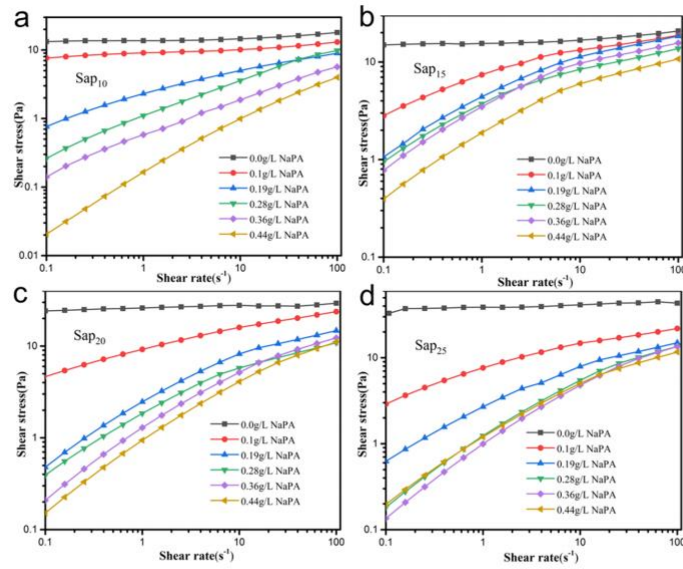
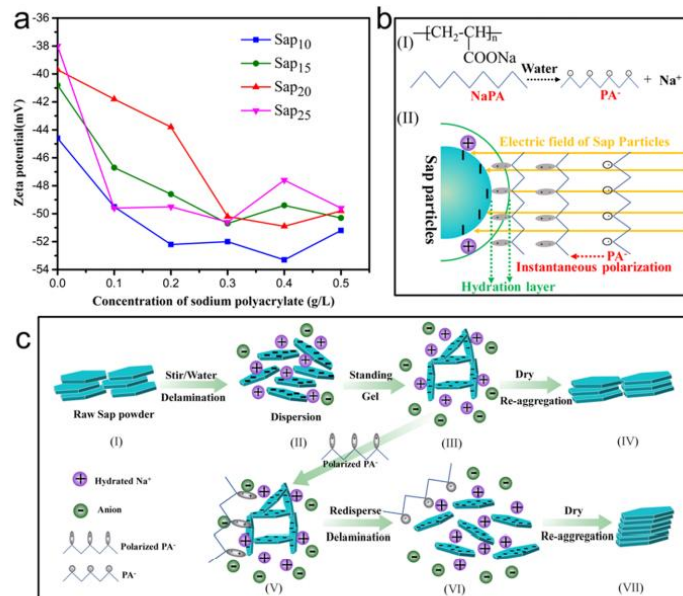


Figure 4. Shear stress as a function of shear rate for (a) Sap<sub>10</sub>-NaPA <sub>$\gamma$</sub> , (b) Sap<sub>15</sub>-NaPA <sub>$\gamma$</sub> , (c) Sap<sub>20</sub>-NaPA <sub>$\gamma$</sub> , and (d) Sap<sub>25</sub>-NaPA <sub>$\gamma$</sub>  dispersions (in the log-log mode), where  $\gamma$  is the addition of NaPA from 0.1 to 0.44 g/L of aqueous Sap dispersion.

675

676



**Figure 5.** (a)  $\zeta$ -Potential of Sap dispersion as a function of sodium polyacrylate (NaPA) concentration. (b) Illustrations of the interactions between Sap particles and sodium polyacrylate (NaPA): (I) Chemical formula of NaPA; (II) interaction between aggregated Sap particle and NaPA. (c) Schematic illustration of Sap dispersion with/without added NaPA and reaggregation after drying: (I) Sap dispersed in water to form (II) Sap dispersion and (III) Sap hydrogel; (V) interaction of the Sap hydrogel with polarized PA to form (VI) Sap-NaPA dispersion; (IV) Sap-control and (VII) Sap-NaPA reaggregated from Sap hydrogel and Sap-NaPA dispersion, respectively.

677  
678

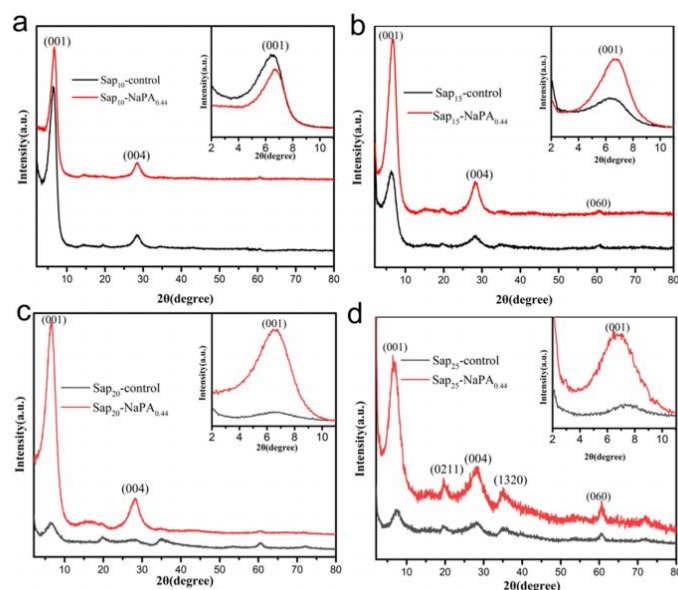


**Figure 6.** Powder XRD patterns of Sap-control and Sap-NaPA<sub>0.44</sub>. Sap-control: dried from Sap<sub>10</sub>, Sap<sub>15</sub>, Sap<sub>20</sub>, and Sap<sub>25</sub> dispersion; Sap-NaPA<sub>0.44</sub>: dried from Sap dispersion after adding NaPA at the concentration of 0.44 g/L.

679

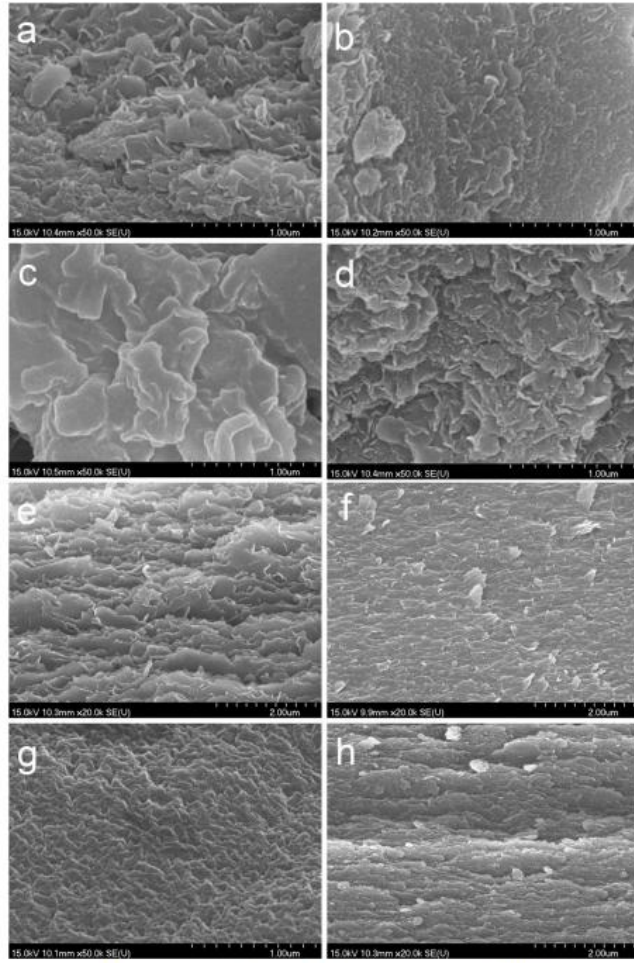


Figure 7. SEM images of (a) Sap<sub>10<sup>0</sup></sub> (b) Sap<sub>15<sup>0</sup></sub> (c) Sap<sub>20<sup>0</sup></sub> (d) Sap<sub>25<sup>0</sup></sub> (e) Sap<sub>10<sup>0</sup></sub>-NaPA<sub>0.44<sup>0</sup></sub> (f) Sap<sub>15<sup>0</sup></sub>-NaPA<sub>0.44<sup>0</sup></sub> (g) Sap<sub>20<sup>0</sup></sub>-NaPA<sub>0.44<sup>0</sup></sub> and (h) Sap<sub>25<sup>0</sup></sub>-NaPA<sub>0.44<sup>0</sup></sub>. Sap<sub>x<sup>0</sup></sub>-NaPA<sub>0.44<sup>0</sup></sub>: dried from Sap dispersion after adding NaPA at the concentration of 0.44 g/L.